

FAIR-ESI: Feature Adaptive Importance Refinement for Electrophysiological Source Imaging

Linyong Zou^{†,1,2}, Liang Zhang^{†,1,2,3}, Xiongfei Wang^{†,4}, Jia-Hong Gao⁵, Yi Sun², Shurong Sheng², Kuntao Xiao², Wanli Yang², Pengfei Teng⁴, Guoming Luan^{*,4}, Zhao Lv^{*,6} and Zikang Xu^{*,2}

¹ School of Artificial Intelligence, Anhui University, Hefei 230601, China.

² Anhui Province Key Laboratory of Biomedical Imaging and Intelligent Processing, Institute of Artificial Intelligence, Hefei Comprehensive National Science Center, Hefei 230088, China.

³ School of Automation, Northwestern Polytechnical University, Xian 710072, China.

⁴ Department of Neurosurgery, Beijing Key Laboratory of Epilepsy, Sanbo Brain Hospital Capital Medical University, Beijing, China.

⁵ McGovern Institute for Brain Research, Peking University, Beijing, China.

⁶ Anhui Province Key Laboratory of Multimodal Cognitive Computation, School of Computer Science and Technology, Anhui University, Hefei 230601, China.

[†] Equal contribution, and * Corresponding authors.

luangm@ccmu.edu.cn, kjlz@ahu.edu.cn, zikangxu@mail.ustc.edu.cn

Abstract—An essential technique for diagnosing brain disorders is electrophysiological source imaging (ESI). While model-based optimization and deep learning methods have achieved promising results in this field, the accurate selection and refinement of features remains a central challenge for precise ESI. This paper proposes FAIR-ESI, a novel framework that adaptively refines feature importance across different views, including FFT-based *spectral* feature refinement, weighted *temporal* feature refinement, and self-attention-based *patch-wise* feature refinement. Extensive experiments on two simulation datasets with diverse configurations and two real-world clinical datasets validate our framework’s efficacy, highlighting its potential to advance brain disorder diagnosis and offer new insights into brain function.

Index Terms—Electrophysiological Source Imaging, Magnetoencephalography, Electroencephalography, Deep Learning

I. INTRODUCTION

Brain disorders, including epilepsy, Parkinson’s disease, and depressive disorder, have brought substantial suffering for a large number of patients all over the world every year [1]. Precise localization of the deep-seated pathological sources of these psychiatric disorders in the brain is critical for developing targeted neuromodulation therapies [2]. However, traditional localization methods, such as stereoelectroencephalography (sEEG), require intracranial electrode implantation, which is expensive and high-risk [3]. Due to the development of neuroimaging technologies, some researchers acquire non-invasive electrophysiological signals from patients’ scalps, such as magnetoencephalography (MEG) and electroencephalography (EEG), followed by source localization algorithms to estimate intracranial activity [4]. This strategy substantially reduces both surgical costs and patients’ discomfort.

Electrophysiological source imaging (ESI) [4] refers to the process of reconstructing brain source activities from scalp

signals, as illustrated in Fig. 1. This technique is inherently an *inverse problem* that reverses the forward propagation model of electromagnetic fields from neural sources to scalp sensors [4]. However, due to the sparse spatial sampling of electromagnetic sensors on the scalp, ESI becomes an ill-posed problem with non-unique solutions [5].

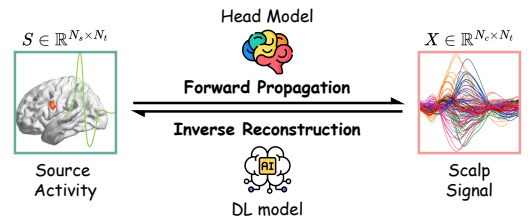


Fig. 1. The forward propagation and inverse reconstruction problem of ESI.

Over the past decades, researchers have attempted to address this ill-posed problem through optimization-based or data-driven algorithms. Traditional optimization-based approaches solve the ESI inverse problem by imposing regularization constraints on the source space to ensure solution uniqueness. While priors in these methods enhance localization accuracy [6]–[9], formulating appropriate regularization constraints remains challenging [10]. Moreover, these methods suffer from two inherent limitations: (1) most of the methods assume static sources, failing to capture transient neural dynamics; (2) the head geometry and tissue conductivity variations require case-specific forward modeling.

To tackle the shortcomings of the traditional methods, some researchers try to solve the ESI problem by adopting deep learning (DL)-based algorithms. By leveraging massive simulated data to tune neural network parameters, DL-based methods can learn more flexible and realistic reconstruction

functions via learning comprehensive spatiotemporal features directly from source-scalp signal pairs [11].

However, current DL-based algorithms tend to treat the following characteristics wrongly when extracting features from the input signals, which leads to inaccurate localization of the source signal: (1) *frequency components*: Brain source activities exhibit distinct electrophysiological signatures across frequency bands, providing discriminative features for ESI [12]. However, most DL models disregard these spectral characteristics, leading to suboptimal feature representation; (2) *temporal samples*: Source spikes induce transient electrophysiological responses on the scalp, where specific time points strongly correlate with underlying neural activity while others contain volume conduction artifacts. Nevertheless, many DL algorithms process entire signal fragments indiscriminately, reducing feature SNR; and (3) *Sub-patches*: Processing full scalp signals introduces spatiotemporal contamination-sub-regions containing activity from preceding/succeeding neural events are erroneously used for source localization. This results in misattribution of signal origins and degraded spatial accuracy.

To solve these issues, in this paper, we propose FAIR-ESI, which improves the precision of ESI by adaptively refining the importance of the extracted features from three different views:

- 1) From the view of *spectral*: FAIR-ESI adopts a Fast Fourier Transform (FFT) [13] based feature refinement strategy which adaptively selects important features in the frequency domain, and then converts the refined feature into the temporal domain;
- 2) From the view of *temporal*: FAIR-ESI applies weighted summation to fuse features in the temporal domain, which can reduce noise while preserving details of the features;
- 3) From the view of *patch-wise*: FAIR-ESI selects the key patch based on energy and enhances it via self-attention, and then this salient feature is propagated across all patches to refine patch-wise features.

Furthermore, paired source-scalp signals are scarce owing to the challenges in simultaneous signal acquisition, which bring difficulties for model training. To solve this problem, we leverage neural mass models (NMMs) [14], which are used to generate brain source activities by numerical simulation, to generate abundant paired data with diverse configurations. As described above, the contributions of this work are as follows:

- 1) An NMM-based method is adopted to simulate paired source-scalp signals with diverse Signal-to-Noise Rate (SNR), number of sources, and number of neighborhood extents, which are used to train the DL-based ESI model;
- 2) A DL model, named FAIR-ESI, which adaptively refines feature importance from three views including *spectral*, *temporal*, and *patch-wise*, is proposed for precise ESI from scalp signals;
- 3) Extensive experiments on two simulation datasets and two real-world clinical datasets prove the effectiveness and generalizability of the proposed model, which also provides potential for automatic brain disorder diagno-

sis, especially for epilepsy.

II. METHODOLOGY

A. Preliminaries

Let $S \in \mathbb{R}^{N_s \times N_t}$ denote the brain source activity in N_s regions of interest (ROIs) at N_t time points, and $X \in \mathbb{R}^{N_c \times N_t}$ denote the corresponding scalp fragments (EEG/MEG) in N_c channels at N_t time points. The forward problem of ESI can be expressed as $X = G \cdot S + N$, where $G \in \mathbb{R}^{N_c \times N_s}$ is the lead-field matrix derived from brain structure, which measures the coupling between a unit current dipole at a specific cortical location and the resultant electromagnetic field measured at each MEG/EEG sensor, and $N \in \mathbb{R}^{N_c \times N_t}$ denotes the measurement noise.

The inverse problem of ESI, which aims to reconstruct the brain source activity S from the observation of EEG/MEG signals, is an ill-posed problem due to the underdetermined nature of the mapping from source space to sensor space. To address this, we aim to learn an end-to-end mapping function P that reconstructs the brain source activity S from the EEG/MEG signals X via DL, i.e., $X \xrightarrow{P} S$.

B. Paired Data Simulation & Patch Data Generation

Because the paired scalp signals X and brain source activities S are precious and rare, following [11], we employ a neural mass model (NMM) to simulate the paired data, which is then used to train our DL model. By adjusting the parameters of the NMM-based Jansen-Rit algorithm [14], we generate a wide range of simulated data with different signal-to-noise rates (SNRs, r), number of sources (N_s), and spatial extents (N_n). Besides, by adopting different head models (Fsaverage2020 [15] and ICBM152 [16]) and lead-field metrics, we can generate both MEG and EEG signals from source activities. This approach allows us to create a diverse dataset that captures the dynamics of neural populations and provides a realistic representation of brain activity.

Unlike previous methods that directly process the entire scalp signal to extract features representing the whole fragment, or splitting the signal into channel-wise segments and generate features for each channel separately, we propose to generate overlapping patches for a more comprehensive patch-wise representation of the signal. This approach allows us to capture patch-wise patterns and enhance the model's ability to learn from the data.

For each scalp fragment $X \in \mathbb{R}^{N_c \times N_t}$, we partition it into channel-independent temporal-overlapped segments, resulting in $P \in \mathbb{R}^{N_c \times N_p}$ patches, where N_p denotes the number of segments for each channel.

C. FAIR-ESI: Feature Adaptive Importance Refinement

To address the aforementioned challenges in the ESI inverse problem, we propose a novel DL algorithm, i.e. FAIR-ESI, which is achieved by adaptively refining the features from the scalp fragments considering the feature importance from *spectral*, *temporal*, and *patch-wise* perspectives.

1) *FFT-based Spectral Feature Refinement*: From a *spectral* point of view, we follow the findings in [12], which hint that some of frequency components are important while usually ignored in the ESI inverse problem. Besides, the background activity in the frequency domain is a common distraction that prevents the model from learning the important features.

For each patch $P(i, j)$, FAIR-ESI first applies the Fast Fourier Transform (FFT) to bring the temporal signal into the frequency domain. Then, the real and imaginary parts of the FFT results are processed separately using a temperature-scaled softmax function to refine the features and remove irrelevant noise, i.e., $\mathcal{T}(x, \tau) = \frac{\exp(x/\tau)}{\sum \exp(x/\tau)}$. After that, an Inverse FFT (IFFT) is adopted to reconstruct the temporal signal from the two components, as shown in Equ. (1).

$$P_S^* = \text{IFFT}(P_{\text{RE}}^*, P_{\text{IM}}^*) = \text{IFFT}(\mathcal{T}(P_{\text{RE}}, \tau), \mathcal{T}(P_{\text{IM}}, \tau)), \quad (1)$$

where $[P_{\text{RE}}, P_{\text{IM}}] = \text{FFT}(P)$ denote the real and imaginary parts of the FFT results, respectively.

2) *Weighted Temporal Feature Refinement*: However, as shown in Fig. 2 (b), the refinement in the spectral domain may result in over-smoothing of the signal, which can cause loss of details in the temporal domain. To address this, we further refine the features from the view of the *temporal* domain.

Specifically, we first use a temperature-scaled softmax function to refine the input patch, i.e., $P_T^* = \mathcal{T}(P, \tau)$. Then, a weighted-summation operation is applied to fuse the refined spectral features P_S^* and the refined temporal features P_T^* , which is expressed as $P^L = \alpha \cdot P_S^* + (1 - \alpha) \cdot P_T^*$, where α is a hyper-parameter that controls the balance between the two components.

3) *Self-Attention-based Patch-wise Feature Refinement*: By the above two steps, we have refined the features for each patch. However, in the whole scalp fragment P with $N_c \times N_p$ patches, not all patches are of equal importance. For example, some patches may contain activated spikes which are critical for source localization, while others may represent resting states which are less relevant. To address this, we propose a cross-attention-based global feature refinement strategy to adaptively fuse the features from all patches.

As shown in Fig. 2 (c), for the patches $P^L(i, j), j \in [1, N_p]$ of the i -th channel, we first compute the element-wise square of each patch. Then, the key patch of the i -th channel, $P^L(i, p)$, is identified as the one with the maximum energy, as shown in $E(i, j) = P^L(i, j) \odot P^L(i, j), \forall j \in [1, N_p]$, where \odot denotes the hadamard product, and $p = \arg \max_j E(i, j)$ is the index of the key patch. Then, we apply self-attention [17] to $P^L(i, j)$ and propagate the attention weights across P^L :

$$Q = W_Q \cdot P_{i,p}^L, K = W_K \cdot P_{i,p}^L, V = W_V \cdot P_{i,p}^L, \quad (2)$$

$$\text{attention} = \text{Softmax}\left(\frac{Q \cdot K^T}{\sqrt{d}}\right) \cdot V, \quad (3)$$

$$P^A = P^F \oplus \text{attention}, \quad (4)$$

where d is the dimension of Q and K , W_Q, W_K, W_V are the projection metrics, and \oplus denotes concatenate operation.

Finally, the attention-enhanced features P^A are sent to two sequential convolutional blocks (Conv2D-ELU-LayerNorm, and TransposeConv2D-ELU-LayerNorm) to obtain the refined features $P^{O*} = \text{TransposeConvBlk}(\text{ConvBlk}(P^A))$.

After repeating this feature adaptive importance refinement procedure for N times, the final output feature P^O is used to reconstruct the source activity.

4) *Source Activity Reconstruction*: Following [11], [18], the refined features, P^{O*} , along with the input scalp signal, X , are fed into the source activity reconstruction module to predict the source activity \hat{S} , as shown in Fig. 2 (d).

For P^{O*} , we employ the same transpose convolutional block to upsample its spatial dimension to match that of the source space, while simultaneously restoring the temporal dimension to its original length.

To preserve essential features in deeper layers, the original input X is projected to the source space dimension via a multi-layer perceptron (MLP). This projection is augmented with a residual branch to mitigate information loss.

Finally, \hat{S} is generated by summing the three components, followed by processing through a bidirectional gated recurrent unit (BiGRU) network [19], as illustrated by Equ. (5).

$$\hat{S} = \text{BiGRU}(\text{TransposeConv}(P^{O*}) + \text{MLP}(X) + X). \quad (5)$$

5) *Loss Function*: The model parameters are optimized iteratively using mean squared error (MSE) loss \mathcal{L} between the predicted source activity \hat{S} and the ground truth source map S , as shown in $\mathcal{L} = \frac{1}{N_s} \|\hat{S} - S\|_F^2$.

III. EXPERIMENTS AND RESULTS

A. Datasets

Both simulation datasets, named as SimMEG and SimEEG, and real-world datasets, including CMR [20] and Localize-MI [21], are used to evaluate the performance of the proposed model.

1) *Simulation Datasets*: Following [11], the Jansen-Rit model is adopted to generate diverse paired data. The details about the two simulation datasets are shown in Table I. For each configuration, we generate 47,904 samples and split them into train, validation, and test sets with a ratio of 10:1:1.

TABLE I
CONFIGURATIONS OF THE SIMULATION DATASETS.

Configurations	SimMEG	SimEEG
Head Model	Fsaverage2020 [15]	ICBM152 [16]
# of Brain regions	998	998
# of Time points	500	260
# of Scalp channels	306	256
# of Sources	1, 2, 3	1
# of Neighborhood Extents	2, 3	2
SNR (dB)	-5, 5, 15	5

2) *Real-world Clinical Datasets*: One private MEG dataset and one publicly-available EEG dataset are used in this study. **CMR Dataset**. The private CMR dataset [20] contains 306-channel MEG recordings and corresponding MRIs from 13

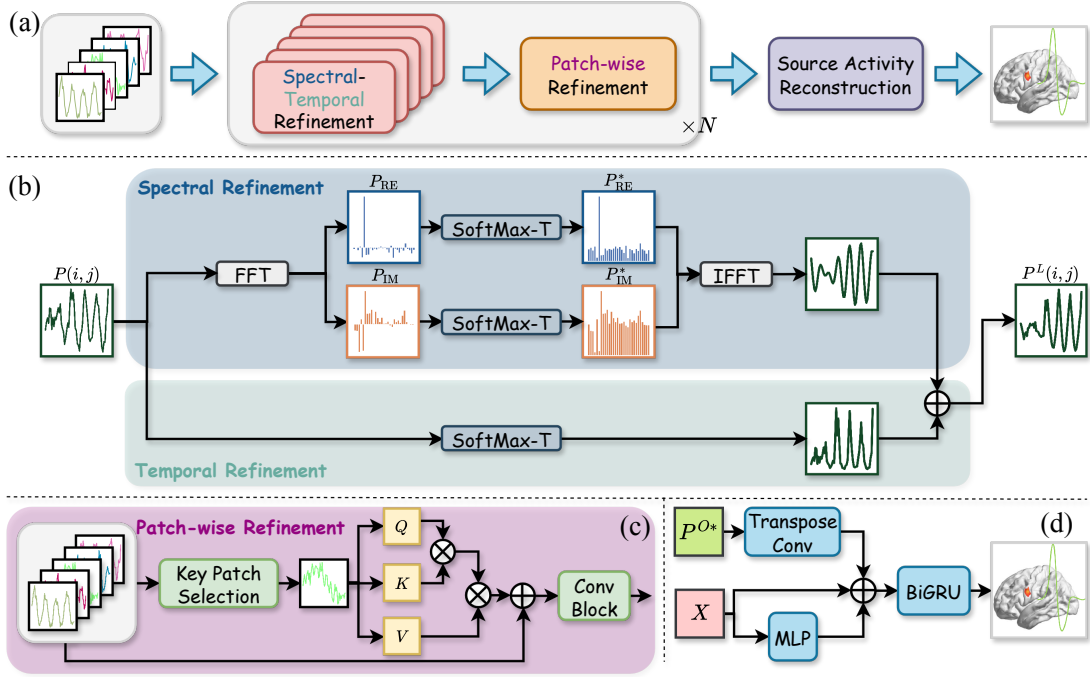


Fig. 2. Overview of FAIR-ESI. (a) The pipeline of the proposed method, which contains three views of feature refinement. (b) Details about spectral-temporal feature refinement. Note that P_{RE}^* and P_{IM}^* are in log-scale for better visualization. (c) Details about patch-wise feature refinement. (d) Details about source activity reconstruction. P^{O*} and X are the output of the feature refinement module and the input scalp signal, respectively.

epilepsy patients. Our study on the CMR dataset was approved by the relevant institutional review boards. Each patient’s MEG recordings are complemented by simultaneous 216-channel stereoelectroencephalography (sEEG) data, which provides definitive ground-truth localization for both seizure-onset zones and interictal epileptiform discharge zones across all brain regions. These labels specifically identify electrophysiologically active areas adjacent to sEEG electrode contacts.

Localize-MI Dataset. The Localize-MI dataset [21] is an open resource featuring high-density EEG data from 61 sessions involving 7 subjects with drug-resistant epilepsy, designed for assessing source localization methods. This dataset provides 256-channel EEG signals at a sampling frequency of 8 kHz, along with spatial coordinates for stimulating brain contacts, which serve as the ground truth for source localization.

B. Experiment Configurations

The proposed FAIR-ESI is optimized using Adam, with a weight decay of $1e-5$. The initial learning rate is set as $1e-4$ and is dynamically reduced by half whenever the test error plateaus until reaching its minimum. The patch length l is set as 16, with an overlap of 8. The temperature of softmax is set as 0.1. The number of FAIR blocks is set as $N = 1$. All experiments are conducted on a Linux server with 8x NVIDIA RTX 4080 Graphics and repeated three times to avoid random errors.

To evaluate the performance of FAIR-ESI, we also implement eight state-of-the-art ESI algorithms in three categories: (1) **Model-based methods:** sLORETA [7], Champagne [22]; (2) **Data-driven methods:** ConvDip [23], DeepSIF [11], SSINet [18], ADMM-ESI [24]; (3) **General time-series methods:** Catch [25], FreEFormer [26]. Following previous studies,

five metrics are adopted to inspect the performance of the models, including precision [11], recall [11], localization error (LE) [11], spatial dispersion (SD) [11], and normalized mean squared error (nMSE) [18]. Specifically, LE measures the minimum distance between the estimated source location and the ground truth region, and SD is used to describe the spatial blurring relative to the ground truth.

C. Quantitative Results

Results on SimMEG dataset. As shown in Table II, for most of simulation configurations, including different SNR, number of sources, and number of neighborhood extents, FAIR-ESI outperforms other state-of-the-art algorithms. This is followed by SSINet [18], which extracts spatial and temporal features simultaneously from scalp fragments. Besides, for the configuration in which the noise is extremely high (SNR=-5 dB), all the other algorithms cannot achieve a precision higher than 80%, while FAIR-ESI results in a precision of 83.99%. This is due to the fact that FAIR-ESI conducts more meticulous feature refinements from diverse views. Besides, although SSINet obtains the highest recall in most of configurations, this occurs because SSINet prioritizes more active sources and facilitates the detection of a larger number of abnormal spikes, which leads to a lower precision.

Extendibility on SimEEG dataset. We also evaluate the extendibility of FAIR-ESI on the SimEEG dataset, which is generated using the same source signal with different head models and lead-field metrics. The results are shown in Table II. As shown in the Table, FAIR-ESI still obtains the best precision, LE, SD, and nMSE metrics among the 9 algorithms, which illustrates good extendibility for ESI using EEG signals. Note that although a 5% drop in precision

TABLE II
RESULTS ON SIMMEG AND SIMEEG DATASETS. ALL EXPERIMENTS WERE REPEATED 3 TIMES, MEAN \pm STD ARE REPORTED. THE BEST AND SECOND BEST RESULTS ARE HIGHLIGHTED. r , N_s , N_n DENOTE THE SNR, NUMBER OF SOURCES, AND NUMBER OF NEIGHBORHOOD EXTENTS, RESPECTIVELY.

r	N_s	N_n	Metrics	sLORETA [7]	Champagne [22]	ConvDip [23]	DeepSIF [11]	SSINet [18]	ADMM-ESI [24]	Catch [25]	FreEFormer [26]	FAIR-ESI	
SimMEG dataset													
-5	1	2	Precision (%)	8.15 \pm 9.39	9.54 \pm 11.10	31.09 \pm 40.61	79.25 \pm 19.19	72.05 \pm 18.12	61.68 \pm 17.12	68.81 \pm 22.37	60.87 \pm 22.62	83.99\pm13.18	
			Recall (%)	18.79 \pm 18.45	19.66 \pm 24.92	20.56 \pm 30.39	83.85 \pm 20.97	92.87\pm12.27	60.87 \pm 30.95	78.99 \pm 24.51	89.19 \pm 16.75	89.19 \pm 16.75	90.09 \pm 12.93
			LE (mm)	80.09 \pm 39.21	66.18 \pm 36.98	<u>2.37\pm4.22</u>	2.88 \pm 7.20	3.03 \pm 3.97	8.61 \pm 9.19	3.50 \pm 4.30	5.89 \pm 8.07	6.18 \pm 7.56	1.96\pm6.04
			SD (mm)	84.31 \pm 38.12	76.12 \pm 41.83	3.42 \pm 4.54	4.18 \pm 7.70	<u>3.35\pm4.13</u>	9.15 \pm 10.57	4.14 \pm 4.54	6.18 \pm 7.56	6.18 \pm 7.56	2.55\pm6.45
			nMSE ($\times 10^{-4}$)	13.32 \pm 4.59	17.54 \pm 8.19	6.30 \pm 4.20	2.49 \pm 2.20	<u>2.36\pm3.56</u>	6.17 \pm 8.40	3.48 \pm 2.61	4.48 \pm 6.34	4.48 \pm 6.34	1.94\pm1.79
5	1	2	Precision (%)	13.19 \pm 16.02	15.63 \pm 18.93	50.11 \pm 33.25	82.20 \pm 16.40	75.14 \pm 16.77	68.59 \pm 15.22	68.18 \pm 24.07	65.93 \pm 19.25	87.18\pm13.74	
			Recall (%)	20.54 \pm 21.64	24.82 \pm 26.31	53.33 \pm 36.70	89.48 \pm 14.37	94.34\pm10.50	75.09 \pm 20.18	73.56 \pm 26.09	88.42 \pm 15.65	88.42 \pm 15.65	92.57 \pm 10.88
			LE (mm)	57.76 \pm 25.21	41.94 \pm 19.69	3.88 \pm 4.09	1.97 \pm 3.11	2.44 \pm 2.63	5.92 \pm 6.73	4.27 \pm 6.32	4.00 \pm 4.27	4.00 \pm 4.27	1.27\pm2.65
			SD (mm)	60.01 \pm 26.43	48.95 \pm 22.78	5.15 \pm 4.22	3.08 \pm 3.83	<u>2.78\pm2.67</u>	6.84 \pm 7.25	5.24 \pm 7.15	4.36 \pm 4.21	4.36 \pm 4.21	1.88\pm2.95
			nMSE ($\times 10^{-4}$)	15.14 \pm 5.69	13.18 \pm 7.75	5.21 \pm 3.51	1.94 \pm 1.87	<u>2.04\pm3.89</u>	5.19 \pm 7.83	4.41 \pm 3.46	2.96 \pm 2.90	2.96 \pm 2.90	1.47\pm1.54
15	1	2	Precision (%)	17.77 \pm 22.52	20.81 \pm 25.53	50.49 \pm 31.46	82.44 \pm 16.59	75.51 \pm 16.60	70.46 \pm 14.81	69.29 \pm 24.25	68.90 \pm 18.63	87.62\pm13.36	
			Recall (%)	21.09 \pm 25.38	28.10 \pm 29.16	56.64 \pm 36.18	89.65 \pm 14.31	94.43\pm10.30	75.82 \pm 19.84	74.21 \pm 25.99	88.61 \pm 15.26	88.61 \pm 15.26	93.60 \pm 9.97
			LE (mm)	37.45 \pm 25.27	26.43 \pm 19.74	4.54 \pm 6.14	1.96 \pm 3.28	2.39 \pm 2.42	5.61 \pm 6.08	4.26 \pm 7.19	3.50 \pm 3.60	3.50 \pm 3.60	1.14\pm1.50
			SD (mm)	38.63 \pm 26.50	31.40 \pm 21.26	5.78 \pm 6.16	3.04 \pm 3.89	<u>2.73\pm2.45</u>	6.78 \pm 7.13	5.25 \pm 8.20	3.95 \pm 3.68	3.95 \pm 3.68	1.75\pm1.82
			nMSE ($\times 10^{-4}$)	10.79 \pm 6.89	11.52 \pm 6.71	5.59 \pm 5.81	1.94 \pm 1.87	<u>2.04\pm2.45</u>	4.97 \pm 7.52	4.13 \pm 3.39	2.70 \pm 2.06	2.70 \pm 2.06	1.38\pm1.47
5	2	2	Precision (%)	11.08 \pm 12.61	13.21 \pm 15.74	51.43 \pm 36.03	81.77 \pm 15.32	79.17 \pm 14.74	62.08 \pm 20.36	59.68 \pm 22.58	64.78 \pm 16.62	88.30\pm12.15	
			Recall (%)	15.66 \pm 16.57	23.04 \pm 25.38	27.12 \pm 23.14	63.64 \pm 22.20	70.37\pm23.40	51.43 \pm 28.90	55.62 \pm 23.64	64.09 \pm 22.93	64.09 \pm 22.93	67.94 \pm 23.37
			LE (mm)	81.73 \pm 47.13	69.92 \pm 44.97	3.51 \pm 4.47	2.16 \pm 3.71	<u>2.09\pm2.33</u>	6.38 \pm 6.92	8.29 \pm 9.01	4.19 \pm 3.72	4.19 \pm 3.72	1.23\pm2.31
			SD (mm)	83.80 \pm 45.57	78.72 \pm 45.84	4.86 \pm 4.59	3.49 \pm 4.15	<u>2.57\pm2.26</u>	9.86 \pm 10.67	9.74 \pm 9.86	4.68 \pm 3.95	4.68 \pm 3.95	1.99\pm2.20
			nMSE ($\times 10^{-4}$)	17.11 \pm 7.04	15.22 \pm 7.87	12.59 \pm 75.18	3.89 \pm 3.64	<u>2.89\pm2.71</u>	9.47 \pm 7.52	7.57 \pm 4.82	4.93 \pm 3.59	4.93 \pm 3.59	2.60\pm2.65
5	3	2	Precision (%)	8.52 \pm 9.61	10.75 \pm 12.64	49.88 \pm 35.02	83.54 \pm 15.95	82.83 \pm 13.67	63.87 \pm 17.69	54.76 \pm 24.57	65.58 \pm 17.85	88.09\pm12.01	
			Recall (%)	13.48 \pm 15.56	20.14 \pm 24.08	22.14 \pm 23.19	60.82 \pm 22.18	66.81\pm23.42	45.91 \pm 31.50	46.61 \pm 22.93	60.90 \pm 22.56	60.90 \pm 22.56	64.82 \pm 22.98
			LE (mm)	85.81 \pm 48.83	78.75 \pm 47.71	4.44 \pm 5.90	2.27 \pm 4.48	1.67 \pm 1.74	6.17 \pm 6.85	11.19 \pm 10.59	4.80 \pm 4.87	4.80 \pm 4.87	1.15\pm1.70
			SD (mm)	88.37 \pm 47.38	89.01 \pm 47.69	5.92 \pm 6.28	3.33 \pm 4.54	<u>2.10\pm1.72</u>	8.92 \pm 9.73	13.31 \pm 11.87	5.06 \pm 4.69	5.06 \pm 4.69	1.75\pm1.91
			nMSE ($\times 10^{-4}$)	18.38 \pm 7.57	17.93 \pm 7.92	11.85 \pm 23.20	4.36 \pm 4.20	<u>3.41\pm3.98</u>	9.92 \pm 8.70	10.18 \pm 6.27	5.73 \pm 4.43	5.73 \pm 4.43	3.08\pm3.37
5	2	3	Precision (%)	4.99 \pm 5.14	8.25 \pm 9.43	49.00 \pm 33.36	81.51 \pm 14.54	78.02 \pm 14.09	59.01 \pm 19.24	56.74 \pm 25.98	64.80 \pm 17.21	85.20\pm12.01	
			Recall (%)	10.17 \pm 15.49	18.17 \pm 22.43	26.55 \pm 21.94	56.73 \pm 21.54	63.54\pm23.55	48.62 \pm 34.16	40.65 \pm 22.43	59.33 \pm 22.53	59.33 \pm 22.53	60.26 \pm 23.03
			LE (mm)	87.72 \pm 49.98	75.19 \pm 46.91	4.71 \pm 5.84	2.20 \pm 3.53	<u>2.16\pm1.89</u>	6.87 \pm 7.22	10.21 \pm 11.09	4.21 \pm 3.55	4.21 \pm 3.55	1.39\pm1.46
			SD (mm)	90.20 \pm 48.21	81.78 \pm 47.17	6.28 \pm 6.12	3.59 \pm 3.91	<u>2.68\pm1.80</u>	8.06 \pm 9.20	12.48 \pm 12.36	4.74 \pm 3.52	4.74 \pm 3.52	2.19\pm1.72
			nMSE ($\times 10^{-4}$)	19.81 \pm 8.73	17.37 \pm 8.03	11.42 \pm 24.17	5.72 \pm 5.36	<u>4.53\pm5.36</u>	10.05 \pm 11.29	11.67 \pm 7.23	6.71 \pm 4.85	6.71 \pm 4.85	4.32\pm4.16
SimEEG dataset													
5	1	2	Precision (%)	12.39 \pm 16.05	12.20 \pm 14.23	43.37 \pm 38.30	78.27 \pm 21.08	70.71 \pm 17.94	62.09 \pm 20.14	54.23 \pm 27.34	59.46 \pm 20.48	81.94\pm18.57	
			Recall (%)	12.55 \pm 16.12	21.45 \pm 24.63	36.89 \pm 35.82	81.24 \pm 23.28	92.93\pm13.07	65.21 \pm 29.11	70.51 \pm 31.63	88.30 \pm 18.14	88.30 \pm 18.14	89.80 \pm 15.40
			LE (mm)	50.82 \pm 28.70	43.96 \pm 20.12	3.44 \pm 4.05	2.92 \pm 7.38	3.12 \pm 3.90	6.85 \pm 8.20	6.39 \pm 7.57	5.17 \pm 5.51	5.17 \pm 5.51	2.03\pm4.24
			SD (mm)	49.65 \pm 36.75	50.93 \pm 23.59	4.74 \pm 4.20	4.20 \pm 7.70	<u>3.50\pm3.87</u>	7.91 \pm 9.18	7.40 \pm 7.98	5.72 \pm 5.69	5.72 \pm 5.69	2.83\pm5.74
			nMSE ($\times 10^{-4}$)	10.53 \pm 3.95	15.17 \pm 7.81	10.36 \pm 41.67	2.68 \pm 2.17	<u>2.35\pm2.22</u>	8.99 \pm 8.85	4.71 \pm 3.80	4.15 \pm 3.22	4.15 \pm 3.22	1.36\pm1.66

(87.18% \rightarrow 81.94%) is observed on the SimEEG dataset compared to the SimMEG results, this is understandable as the SimEEG task involves localizing the source from 256-channel signals, whereas the SimMEG dataset utilizes 306-channel MEG signals.

Generalizability on Real-world Datasets. Furthermore, we evaluate FAIR-ESI on the two real-world datasets, to see if the proposed method can generalize to more complex tasks in clinical trials. Following [11], spatial dispersion is used as the metric. As shown in Table III, FAIR-ESI outperforms other sota algorithms on both of the datasets. This is because that by adaptively refining the feature importance from different views, FAIR-ESI learns a better representation from scalp signals, which helps capture key features for ESI.

D. Qualitative Results

To better illustrate the differences among the 9 algorithms, qualitative results on simulation and real-world datasets are presented in Fig. 3 and Fig. 4.

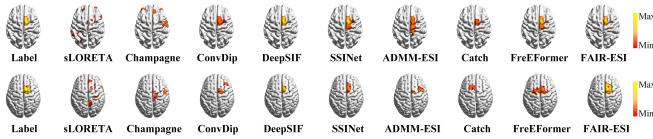


Fig. 3. Visualization of SimMEG and SimEEG datasets, the simulated source is located at region 121. Upper: SimMEG with $[r, N_s, N_n] = [5, 1, 2]$; Lower: SimEEG with $[r, N_s, N_n] = [5, 1, 2]$. Colors represent the amplitude of the estimated source activation.

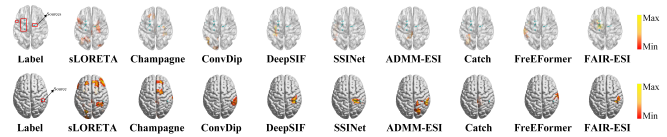


Fig. 4. Visualization of CMR and Localize-MI datasets. Upper: CMR dataset; Lower: Localize-MI dataset. Colors represent the amplitude of the estimated source activation.

Visualization of Source Localization. As shown in Fig. 3, compared to other methods, FAIR-ESI demonstrates the highest consistency with the real labels. Note that while FreEFormer achieves coarse source localization, its inability to precisely estimate signal intensity introduces errors in downstream source signal analysis. Similar results are found on the two real-world datasets. Whereas FAIR-ESI can accurately localize the source signal, sLORETA completely fails to localize source signals due to its lack of multi-view refinement for extracted features.

Visualization of Spectral-Temporal Refinement. Fig. 5 (a) illustrates the features before and after the spectral-temporal refinement. While spectral refinement enhances targeted frequency bands at the expense of signal details, the subsequent temporal refinement mitigates this through weighted feature fusion, ultimately achieving superior feature representation.

Visualization of Key-patch selection. As for the patch-refinement, Fig. 5 (b) presents the energy-based selection of key-patches. From the figure we can find that the spike events

TABLE III

MEAN SPATIAL DISPERSION OF CMR AND LOCALIZE-MI DATASET. ALL EXPERIMENTS WERE REPEATED 3 TIMES, MEAN \pm STD ARE REPORTED. THE BEST AND SECOND BEST RESULTS ARE HIGHLIGHTED.

Dataset	sLORETA [7]	Champagne [22]	ConvDip [23]	DeepSIF [11]	SSINet [18]	ADMM-ESI [24]	Catch [25]	FreEFormer [26]	FAIR-ESI
CMR	109.68 \pm 32.81	86.31 \pm 27.94	89.34 \pm 51.25	40.38\pm21.68	49.81 \pm 30.97	92.58 \pm 31.44	76.32 \pm 26.86	60.17 \pm 25.60	32.55\pm17.19
Localize-MI	80.47 \pm 12.35	69.33 \pm 15.71	55.68 \pm 21.84	31.49\pm10.82	34.65 \pm 19.30	70.62 \pm 26.57	61.14 \pm 22.09	53.75 \pm 14.35	22.86\pm6.34

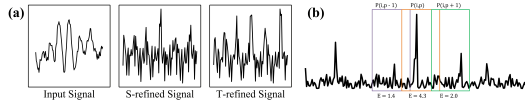


Fig. 5. (a) Visualization of spectral-temporal feature refinement; (b) Visualization of key-patch selection, E denotes the energy of the patch.

generally occupy the highest energy, thus are more likely to be chosen as key-patches. This results in reasonable refinement from a patch-wise perspective.

E. Ablation Studies

Ablation on Refinement Views. To further evaluate the impact of the feature refinement in each view, we conduct ablation experiments on the SimMEG dataset with $r = 5$, $N_s = 2$, $N_n = 2$. The results are shown in Table IV. As shown in the Table, by combining the three views of feature refinement, FAIR-ESI achieves the best precision, LE, and nMSE, with comparable Recall and SD.

TABLE IV
ABLATION STUDY ON FEATURE REFINEMENT VIEWS.

Refinement Views			Precision	Recall	LE (mm)	SD (mm)	nMSE
Spectral	Temporal	Patch-wise	(std)	(std)	(std)	(std)	(std)
			81.22 (13.48)	68.95 (23.46)	1.79 (1.74)	2.32 (1.77)	3.02 (2.94)
✓			80.83 13.94	67.63 23.25	1.80 1.58	2.29 1.63	3.04 2.83
	✓		80.20 14.15	66.38 23.20	1.84 1.54	2.29 1.56	3.27 4.16
✓	✓		83.99 (13.23)	67.943 (23.21)	1.53 (1.72)	2.13 (1.85)	2.95 (2.68)
		✓	82.76 (13.42)	68.05 (23.36)	1.67 (1.94)	1.94 (2.08)	2.97 (2.83)
✓	✓	✓	88.30 (12.15)	67.94 (23.83)	1.23 (2.31)	1.99 (2.20)	2.60 (2.62)

IV. CONCLUSION

This paper introduces FAIR-ESI, which improves the precision of ESI by adaptively refining the importance of extracted features from three different views, including *spectral*, *temporal*, and *patch-wise*. Extensive experiments on the simulation and real-world datasets reflect the effectiveness of the proposed method, which provides the potential for further evaluations on the functionalities of the brain and the mechanism of brain disorders.

REFERENCES

- [1] World Health Organization. *Neurological disorders: public health challenges*. World Health Organization (WHO), 2006.
- [2] Timothy O Laumann et al. Precision neuroimaging for localization-related psychiatry. *JAMA psychiatry*, 80(8):763–764, 2023.
- [3] Andre R Brunoni et al. Noninvasive brain stimulation in psychiatric disorders: a primer. *Brazilian Journal of Psychiatry*, 41:70–81, 2018.
- [4] Bin He et al. Electrophysiological source imaging: a noninvasive window to brain dynamics. *Annual review of biomedical engineering*, 20(1):171–196, 2018.
- [5] Meng Jiao et al. XDL-ESI: Electrophysiological Sources Imaging via explainable deep learning framework with validation on simultaneous EEG and iEEG. *NeuroImage*, 299:120802, 2024.
- [6] Anders M. Dale et al. Dynamic Statistical Parametric Mapping: Combining fMRI and MEG for High-Resolution Imaging of Cortical Activity. *Neuron*, 26(1):55–67, 2000.
- [7] R.D. Pascual-Marqui. Standardized low resolution brain electromagnetic tomography (SLORETA): Technical details. *Methods and findings in experimental and clinical pharmacology*, 24 Suppl D:5–12, 2002.
- [8] Sebastián Castaño-Candamil et al. Solving the EEG inverse problem based on space–time–frequency structured sparsity constraints. *NeuroImage*, 118:598–612, 2015.
- [9] Li Zheng et al. Enhanced Fast-VESTAL for Magnetoencephalography Source Imaging: From Theory to Clinical Application in Epilepsy. *IEEE Transactions on Biomedical Engineering*, 68(3):793–806, 2021.
- [10] Rui Sun et al. Deep learning based source imaging provides strong sublobar localization of epileptogenic zone from meg interictal spikes. *NeuroImage*, 281:120366, 2023.
- [11] Rui Sun et al. Deep neural networks constrained by neural mass models improve electrophysiological source imaging of spatiotemporal brain dynamics. *Proceedings of the National Academy of Sciences*, 119(31):e2201128119, 2022.
- [12] Zhengxiang Cai et al. Noninvasive high-frequency oscillations riding spikes delineates epileptogenic sources. *Proceedings of the National Academy of Sciences of the United States of America*, 118(17), April 2021.
- [13] E. O. Brigham et al. The fast fourier transform. *IEEE Spectrum*, 4(12):63–70, 1967.
- [14] Michael Breakspear. Dynamic models of large-scale brain activity. *Nature Neuroscience*, 20:340–352, 2017.
- [15] Bruce Fischl et al. High-resolution intersubject averaging and a coordinate system for the cortical surface. *Human brain mapping*, 8(4):272–284, 1999.
- [16] John C Mazziotta et al. A probabilistic atlas of the human brain: theory and rationale for its development. *Neuroimage*, 2(2):89–101, 1995.
- [17] Ashish Vaswani et al. Attention is all you need. *Advances in neural information processing systems*, 30, 2017.
- [18] Wuxiang Shi et al. A deep learning framework leveraging spatiotemporal feature fusion for electrophysiological source imaging. *Computer Methods and Programs in Biomedicine*, 266:108767, 2025.
- [19] Chao Li et al. BiGRU network for human activity recognition in high resolution range profile. In *2019 International radar conference (RADAR)*, pages 1–5. IEEE, 2019.
- [20] Li Zheng et al. An artificial intelligence–based pipeline for automated detection and localisation of epileptic sources from magnetoencephalography. *Journal of Neural Engineering*, 20(4):046036, 2023.
- [21] Ezequiel Mikulan et al. Simultaneous human intracerebral stimulation and hd-eeeg, ground-truth for source localization methods. *Scientific data*, 7(1):127, 2020.
- [22] Chang Cai et al. Bayesian algorithms for joint estimation of brain activity and noise in electromagnetic imaging. *IEEE Transactions on Medical Imaging*, 42(3):762–773, 2023.
- [23] Lukas Hecker et al. ConvDip: A convolutional neural network for better eeg source imaging. *Frontiers in Neuroscience*, 15:569918, 2021.
- [24] Ke Liu et al. Admm-esinet: A deep unrolling network for eeg extended source imaging. *IEEE Journal of Biomedical and Health Informatics*, pages 1–11, 2025.
- [25] Xingjian Wu et al. CATCH: Channel-aware multivariate time series anomaly detection via frequency patching. In *ICLR*, 2025.
- [26] Wenzhen Yue et al. FreEFormer: Frequency Enhanced Transformer for Multivariate Time Series Forecasting. *arXiv preprint arXiv:2501.13989*, 2025.